
**AFRL-AFOSR-UK-TR-2022-0024**

# Avian-Inspired Multifunctional Morphing Air Vehicles: Underpinning Biological Research

**Bomphrey, Richard**
**THE ROYAL VETERINARY COLLEGE**
**4 ROYAL COLLEGE STREET**
**LONDON, , NW1 0TU**
**GBR**

**02/17/2022**
**Final Technical Report**



Air Force Research Laboratory
Air Force Office of Scientific Research
European Office of Aerospace Research and Development
Unit 4515 Box 14, APO AE 09421

# REPORT DOCUMENTATION PAGE

**PLEASE DO NOT RETURN YOUR FORM TO THE ABOVE ORGANIZATION.**

| 1. REPORT DATE | 2. REPORT TYPE | 3. DATES COVERED | |
|---|---|---|---|
| 20220217 | Final | START DATE<br>20151101 | END DATE<br>20211031 |

**4. TITLE AND SUBTITLE**
Avian-Inspired Multifunctional Morphing Air Vehicles: Underpinning Biological Research

| 5a. CONTRACT NUMBER | 5b. GRANT NUMBER | 5c. PROGRAM ELEMENT NUMBER |
|---|---|---|
| | FA9550-16-1-0034 | 61102F |
| **5d. PROJECT NUMBER** | **5e. TASK NUMBER** | **5f. WORK UNIT NUMBER** |
| | | |

**6. AUTHOR(S)**
Richard Bomphrey

**7. PERFORMING ORGANIZATION NAME(S) AND ADDRESS(ES)**
THE ROYAL VETERINARY COLLEGE
4 ROYAL COLLEGE STREET
LONDON NW1 0TU
GBR

**8. PERFORMING ORGANIZATION REPORT NUMBER**

| 9. SPONSORING/MONITORING AGENCY NAME(S) AND ADDRESS(ES) | 10. SPONSOR/MONITOR'S ACRONYM(S) | 11. SPONSOR/MONITOR'S REPORT NUMBER(S) |
|---|---|---|
| EOARD<br>UNIT 4515<br>APO AE 09421-4515 | AFRL/AFOSR IOE | AFRL-AFOSR-UK-TR-2022-0024 |

**12. DISTRIBUTION/AVAILABILITY STATEMENT**
A Distribution Unlimited: PB Public Release

**13. SUPPLEMENTARY NOTES**

**14. ABSTRACT**
Designs for aerial vehicles based on inspiration from nature is a concept that has been effective for over a hundred years. Early pioneers recognised control authority to be a greater challenge than the generation of lift and thrust, and used wing warping to solicit asymmetric forces and torques. In the interim, wing flexibility as a facilitator of flight control has been neglected in favour of more tractable rigid body dynamics. More recently, the benefits of wing morphing are being revisited with bio-inspiration again playing a key role in the identification of innovations that can produce step-changes in capability. The ability to modulate forces and torques on the airframe by smooth and continuous variation in lifting surface morphology has long been exhibited by birds. For vehicles it confers significant advantages for control, flight performance, fuel economy and reduced radar visibility.

**15. SUBJECT TERMS**

| 16. SECURITY CLASSIFICATION OF: | | | 17. LIMITATION OF ABSTRACT | 18. NUMBER OF PAGES |
|---|---|---|---|---|
| a. REPORT | b. ABSTRACT | c. THIS PAGE | | |
| U | U | U | SAR | 34 |

| 19a. NAME OF RESPONSIBLE PERSON | 19b. PHONE NUMBER *(Include area code)* |
|---|---|
| SHAD REED | 314-235-6179 |

# Avian-Inspired Multifunctional Morphing Air Vehicles: Underpinning Biological Research

Professor Richard J Bomphrey & Professor James R Usherwood

*Prepared by Dr Jorn A Cheney*

*Structure and Motion Laboratory*

*Royal Veterinary College, University of London*

Email: rbomphrey@rvc.ac.uk

# 1 Abstract

Designs for aerial vehicles based on inspiration from nature is a concept that has been effective for over a hundred years. Early pioneers recognised control authority to be a greater challenge than the generation of lift and thrust, and used wing warping to solicit asymmetric forces and torques. In the interim, wing flexibility as a facilitator of flight control has been neglected in favour of more tractable rigid body dynamics. More recently, the benefits of wing morphing are being revisited with bio-inspiration again playing a key role in the identification of innovations that can produce step-changes in capability. The ability to modulate forces and torques on the airframe by smooth and continuous variation in lifting surface morphology has long been exhibited by birds. For vehicles it confers significant advantages for control, flight performance, fuel economy and reduced radar visibility.

# 1 Goals

Deliver detailed information on the way in which birds morph their shape in response to a number of perturbations that change loading on their wings in gliding flight. The perturbations will be either rapid or fixed, symmetrical or asymmetrical, and around multiple axes. The output will be implementable in unmanned air systems that utilize shape memory alloys for large-scale motions and piezoelectric actuators for high-frequency responses.

# 2 Background – Avian Inspiration

Previous research in morphing wings has shown distinct advantages over conventional flight control surfaces. Initially motivated by the casual observation of flight control motions made by birds, morphing research has proceeded without much understanding of how and why birds use their wings for flight control. Nor has previous research made use of the full spectrum of active materials, advances in neuromorphic computing or distributed sensing. The proposed research is to understand how morphological and kinematic parameters of bird wings determine unsteady aeromechanics and flight dynamics and to use the data to inform the appropriate use of novel active materials, distributed sensing and control, structural integration, and neuromorphic circuits to build new concepts of morphing wings.

Birds can inspire a step change in the flight performance of autonomous air vehicles by drawing on 150 million years of R&D through natural selection. They provide scalable solutions, suitable for a broad range of autonomous platforms. Wingspans range from two inches to twelve feet, with extinct birds exhibiting spans of 25 feet (*Argentavis magnificens*: 6-8 million years ago). The mass of today's flying birds extends over four orders of magnitude: 1.5g – 20kg. Birds vary greatly in airspeed, with peregrine falcons reportedly travelling over 120 miles per hour, while hummingbirds can hover and even fly backwards. Geese have the musculature and power output required to hover for a few seconds but are also known to cruise at altitudes of 30,000 feet.

Bird morphology varies between species, but all birds share the same basic muscular-skeletal anatomy by virtue of their common ancestor and control their flight by warping and deforming their wings and tails. Those control surfaces are made from a complex, but tractable, arrangement of

bone, muscle, cartilage, ligament, tendon, skin and feathers. The surfaces are usually continuous with no aileron-like discontinuities that can lead to unwanted flow separation, loss of control and a reduction in flight efficiency. Furthermore, whether passive or active, actuation can be very rapid, enabling wing morphing for planned manoeuvres or in response to atmospheric disturbances to be effective within the blink of an eye.

# 3 Aims

For a set of large bird species, measure gliding wing form under flight conditions that elicit either rapid or slow-adapting changes in wing form:

1. Measure steady or slow-adapting wing forms during
    a. steady glides in still air
    b. lift-enhancement due to constant ground-effect
2. Measure rapid wing morphing due to
    a. Vertical gusts
    b. rotational gusts
3. Understand avian gust rejection
    a. Identify the key components of wing morphing that allow for gust rejection.
    b. Model the aeromechanics necessary for effective gust rejection
    c. Test the effectiveness of the avian-inspired gust-rejection mechanism in a glider.
4. Estimate aerodynamic force production using computational fluid dynamics
    a. Rigorous validation of our computational fluid dynamics as related to avian flight
5. Examine the role of the tail in flight efficiency using computational fluid dynamics

# 4 Methods

We will train large birds to glide over, and through, a suite of apparatus in the Structure and Motion Laboratory at the Royal Veterinary College. We will use a variety of birds handled by their trainers as well as RVC staff. We previously proposed to study three birds, but we have expanded the study to contain five well-performing species: Goshawk, Raven, Tawny Eagle, Barn Owl, and Tawny Owl (**Fig. 1**). The birds will be sourced from Lloyd and Rose Buck (www.lloydbuck.co.uk). These birds fly well under experimental conditions, can carry harnesses that hold instrumentation, and are well behaved (**Fig. 2**). We will subject the birds to a series of perturbations that either rapidly or slowly alter aerodynamic loading on the wings, either symmetrically or asymmetrically.

***Figure 1*** *Gliding birds in the experimental flight corridor. Stitched image of Barn Owl (left) and Tawny Owl (right) utilizing similar flexed-wing configurations during gliding in ground-effect.*

***Figure 2*** *Birds are well-trained and amenable to working in new environments. For example, they are comfortable being held by members of the research team, which simplifies future manipulations. Above, a Tawny Owl is held by Lt. Col. Reed.*

Measurements of wing shape will be acquired using ten to fourteen high-speed cameras. The cameras will form sets of pairs split above and below the birds. Each camera pair provides a disparity map (with sub-pixel resolution) used to reconstruct a dense cloud of markers representing the wing surface.

Dense point clouds lack frame-to-frame coherence, so to identify general wing regions and define consistent local-coordinate systems for analyses, we reconstruct reference markers using a motion capture system (Qualisys inc.). An array of retroreflective markers will be placed on the body, wings, and tail, which will allow us to understand how wing, tail, and body deform relative to one another in response to perturbations.

Experiment 1 manipulates vertical loading by providing birds with constant ground-effect lift enhancement. Wing form during ground-effect gliding will be compared to wing form out of ground effect. To capture the images necessary for these measurements, we elevate the "ground" to allow

camera placement beneath it for filming the bird's ventral surface. Two meters of an 18m long flight corridor contain a transparent floor for imaging, the additional corridor is to allow the bird to gather speed (**Fig. 3**).

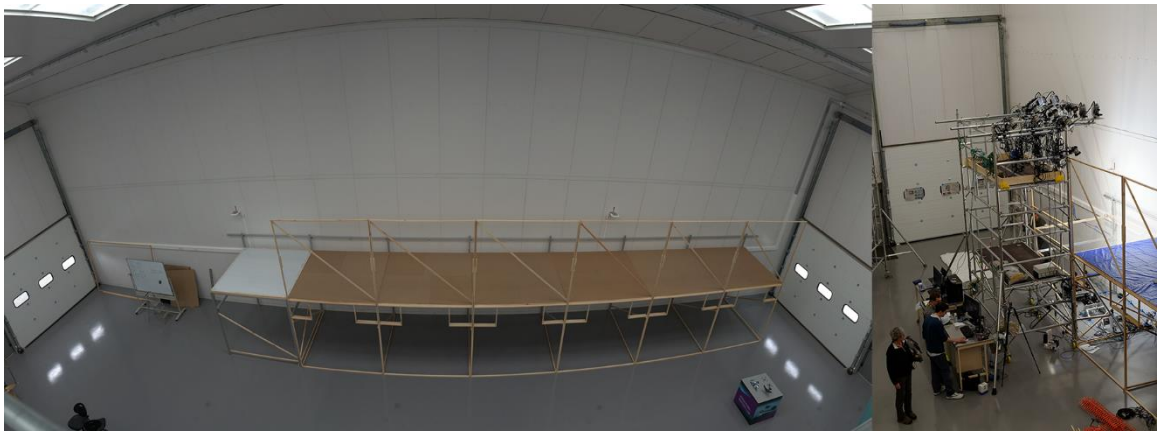

***Figure 3*** *(Left) View of 14m of the flight corridor within barn (4m of the corridor have been removed). The flight path is straight and constrained by the barn wall and a mesh wall. Twelve meters of the corridor contain an opaque floor (brown, left; blue, right), while the last two meters contain either a transparent section (for ground-effect aerodynamic enhancement), a gap for control flights, or a gust generator. In the panels above, the transparent floor is in place, and is protected by a white laminate when not in use. (Right) A four-meter tall scaffold unit holds the motion-capture system and high-speed cameras responsible for imaging the dorsum of the bird. The scaffold is placed in front of the measurement volume and the opaque floor is now covered in a blue waterproof film.*

Experiment 2 dynamically manipulates vertical loading on the bird by means of a strong, channelled gust. The measurement volume surrounds the gust, in order to capture dynamics before entering the gust, during, and the recovery response. To capture this range of behaviours, we extended the measurement volume length from 2 meters to 3.5 meters. The upward gust channel measures 0.6 x 1.6 m--channel width is slightly less than the whole corridor span to allow access points, and flow speeds are nominally set to 0, 3, 4.5, and 5.5 m/s. We determined sufficient gust speeds by iteratively increasing flow speed and perturbing the flights, 5.5 m/s is sufficient, without being dangerous to the animal or hindering wing shape measurement, to elicit dynamic morphing in all of our study species (**Fig. 4**). The Tawny Owl was not studied in this experiment because of death, a new Tawny Owl will be used in future studies once mature.

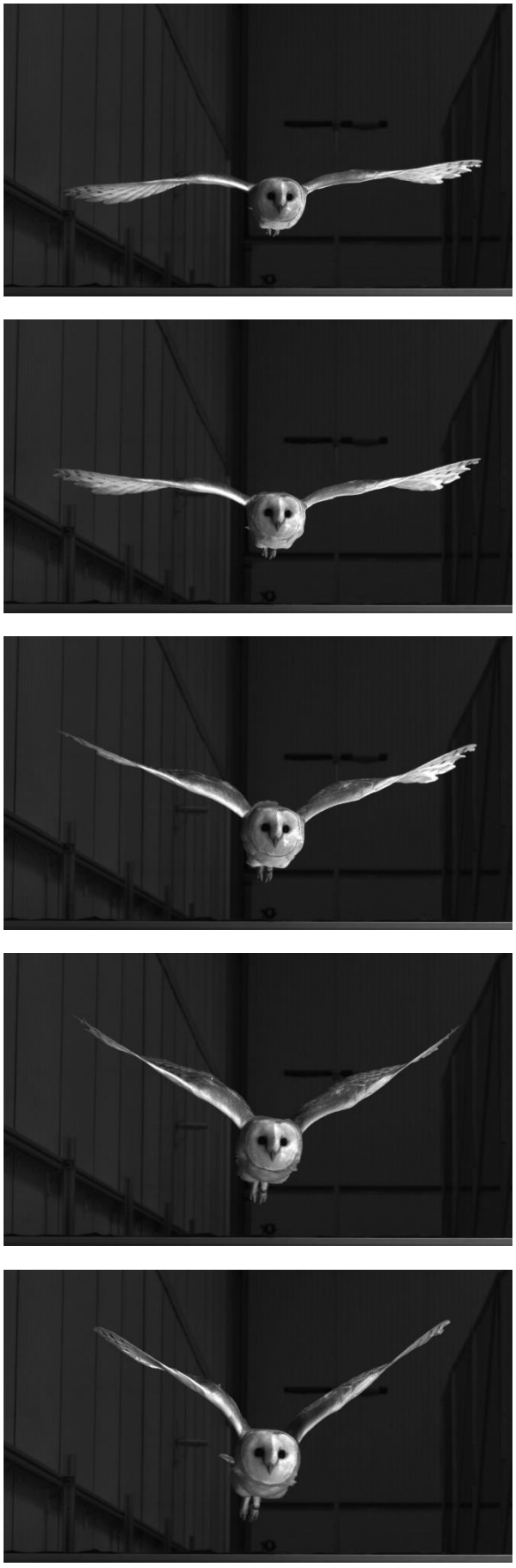

***Figure 4*** *Representative vertical maximum gust response. Sequence of five images over 80 ms demonstrating the dramatic wing morphing in response to the upward gust. Birds respond to the gust at multiple scales: at the level of the skeleton, the wing rotates at the shoulder reducing the relative oncoming flow speed; at the level of the feather, the trailing edge passively deflects reducing the wing's angle of attack. The trajectory of the bird is essentially unchanged in response to these morphing behaviours.*

Experiment 3 provides a rolling torque induced by one or more gust generators measuring 0.6 x 0.8m in order to perturb a single wing (**Fig. 5**). In this experiment, we induced similar aerodynamic moments by providing an upward gust on the right wing, a downward gust on the left wing, and through a combination of the two gusts. We varied gust intensity across a range of speeds. A rigid-winged aircraft could have experienced approximately the same torque in all three perturbations; however, the shoulder of birds is expected to respond differently due to the musculoskeletal system anchoring the wing. An upward gust should be resisted by the pectoralis, while a downward gust must have the pectoralis deactivate. The length of our measurement volume was approximately 2.5 meters, as we found extending it to 3.5 meters in experiment 2 reduced accuracy slightly. The measurement volume surrounds the gust, in order to capture dynamics before entering the gust, during, and the recovery response. Air speeds were up to 5 m/s. We collected measurements from the Barn Owl, Goshawk, and Tawny Eagle in this experiment; the Tawny Owl was not yet mature, and the Raven was excluded due to behavioural reasons likely induced by the presence of the massive gust generator.

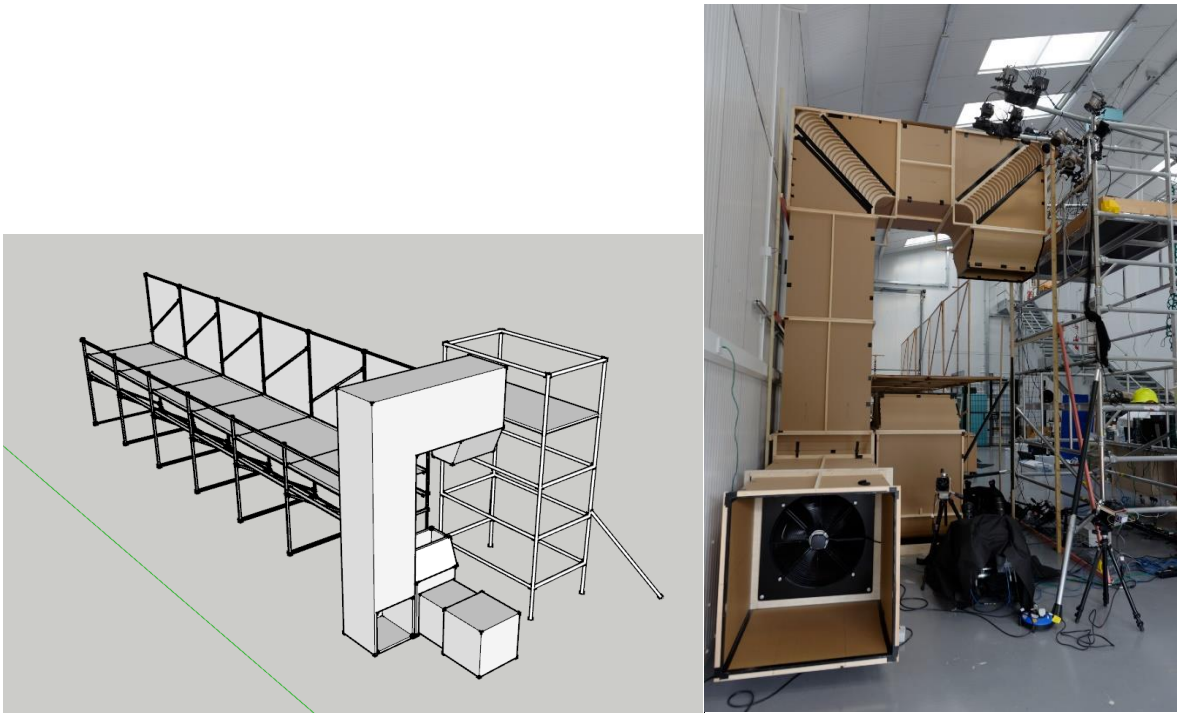

***Figure 5. rolling-gust generator*** *left) CAD model of gust-induced rolling-torque generator; right) gust generator and camera configuration during experiment. The gusts induce roll either through 1) a downward gust on the left wing, 2) an upward gust on the right wing, or 3) a combination of the two gusts. Despite similar torques on the bird, the musculoskeletal system will respond differently and induce different wing morphs.*

To understand the effects of wing configuration we will perform computational fluid dynamics (CFD). We will generate mesh models of the birds from the measured poses and 1) deform the models to infer the effects of wing pose and shape, and 2) deform the models to match the poses as they deform through time to understand the control approaches used by birds. We will validate the CFD studies by comparing the computed flow to the measured flow in steady glides. In collaboration with LaVision, we will track the movement of the flow as the birds glide through air seeded with ~300 micron, neutrally-buoyant soap bubbles.

Finally, we will measure wing morphing in free-flight using a backpack carrying an array of sensors. The Golden Eagle will soar/glide outside of the lab and is capable of carrying substantial loads. We will equip the Golden Eagle with a 6-axis accelerometer, pressure sensor, GPS, magnetometer, and 360° camera with microphone. These sensors allow us to relate wing movements to behavioural phenomena. We plan to test whether wing tucks in the Golden Eagle correlate with downward body acceleration with some brief phase delay induced by the wings accelerating mass.

We will inform our interpretation of avian perturbation responses by examining musculoskeletal anatomy. We will use the diagnostic imaging suite available at the RVC to determine the anatomy of the experimental birds with a high degree of detail and accuracy. By performing the scans in conjunction with similar materials of known density, we can accurately estimate distribution of mass throughout the birds. Mass distribution determines centre of mass, and when combined with centre of lift provides insight into the kinematic response to wing morphing. Further, through knowledge of segment mass, the internal inertial forces caused by wing morphing can provide insight into inertial responses to wing movement. This information is essential to inform bio-inspired morphing wings.

# 5 Collaborative Developments

We ran multiple experiments with our collaborator Dr. Shane Windsor at the University of Bristol. This collaboration has doubled the number of high-speed cameras available for reconstructing wing form and leveraged their knowledge of avian photogrammetry.

We shared our wing profiles with Prof. Darren Hartl and provided Prof. Dan Inman with the dynamics of the tail. Prof. Hartl is developing actuators and is using the information to gauge the magnitude of morphing needed for his wing design. Prof. Inman has developed a morphing tail and will use our dynamics to inform how his actuated design might be used in a morphing aircraft.

# 6 Accomplishments

- Conducted measurement error analysis for high-speed videogrammetry.
- Developed high-speed high-power stroboscopic LEDs for imaging indoors with sufficiently high shutter speeds (1/2000-1/5000) to prevent motion blur at high relative magnifications.
- Completed construction of flight corridor with elevated floor and videogrammetric capture zone.
- Developed and characterized a vertical gust channel with sufficient flow speeds and channel size to perturb all study species.
- Designed and constructed a torque-inducing gust generator with multiple mechanisms to induce a rolling moment.
- Used an array of twelve high-speed cameras to acquire a dense (few hundred thousand points per exposure) point cloud of the ventral (lower) and dorsal (upper) surfaces of five bird species during glides in and out of ground effect.

- Used an array of ten high-speed cameras to acquire dense point clouds, similar to above, of five bird species encountering a vertical gust.
- Used an array of fourteen high-speed cameras to acquire dense point clouds, similar to above, of three bird species encountering rolling gusts.
- Used motion capture to acquire a sparse array of anatomical markers during glides in both experiments.
- Processed all images from experiment 1 and 2 to produce dynamic surface reconstructions. We have tested reconstruction of experiment 3 and we anticipate no problems.
- Segmented the surfaces of the wings, tail, and body, for experiment 1 and 2 and developed approaches to identify both the gross postural changes of the segments over time or across trials, and through re-mapping of the surfaces, we can identify the fine-scale surface changes.
- Compared gross postural changes between control flight and ground-effect flights.
- Analyzed wing and torso movements when encountering an upward gust and have developed a multi-phase response to explain gust rejection in birds.
- Meshed an exemplar instance of the Barn Owl in flight.
- Computed flows using ANSYS around the Barn Owl.
- Measured the flow around the Barn Owl, Tawny Owl, and Goshawk during steady glides.

# 7 Results

**Reconstructions**

Typical dense point cloud reconstructions are performed with high-spatial resolution colour cameras designed to capture still images with little to no temporal resolution. Our reconstructions performed with relatively low-resolution (1-4MP) high-speed monochrome cameras have reduced accuracy, but provide a dynamic record of bird wing deformations in flight. To estimate our error, we used a dense point cloud reconstruction of a fibreglass bird model against a high-accuracy laser scan. In experiment 1, our median absolute error is below one millimetre, with a non-Gaussian distribution (**Fig. 6**). Birds in flight can be more difficult to reconstruct due to motion blur and feather level patterning. However, reconstructions reveal that our newly developed high-powered strobe lights are sufficiently bright to capture sharp, fine features across the bird, and that reconstruction quality is likely similar to the static fibreglass model (**Fig. 7**).

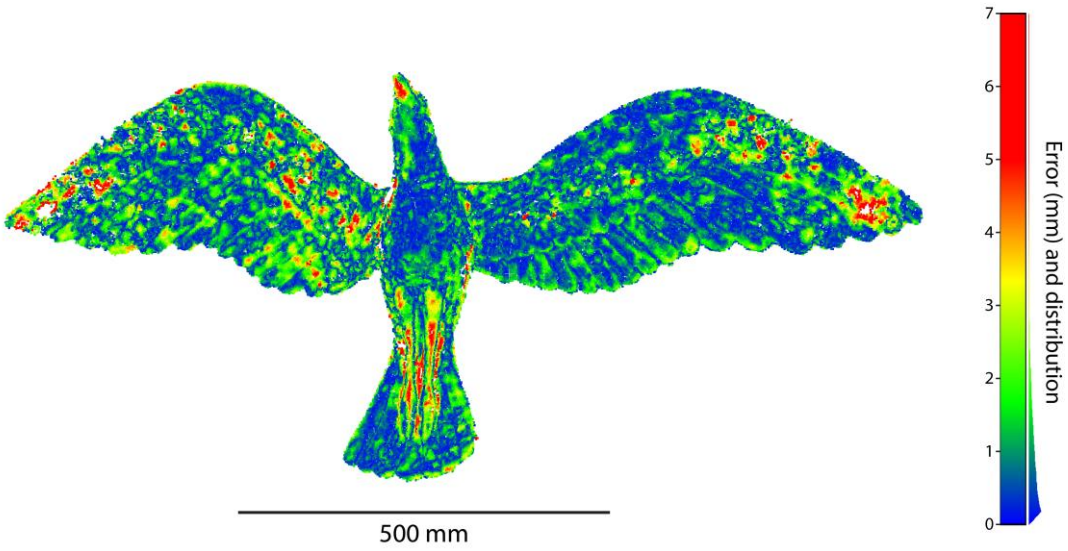


***Figure 6*** *Error in videogrammetric reconstruction of a rigid laser-scanned bird model. Reconstructed point cloud is color-coded based on absolute error. Error distribution is right of the colour bar. Reconstruction performed with identical camera and light placement used during data collection.*

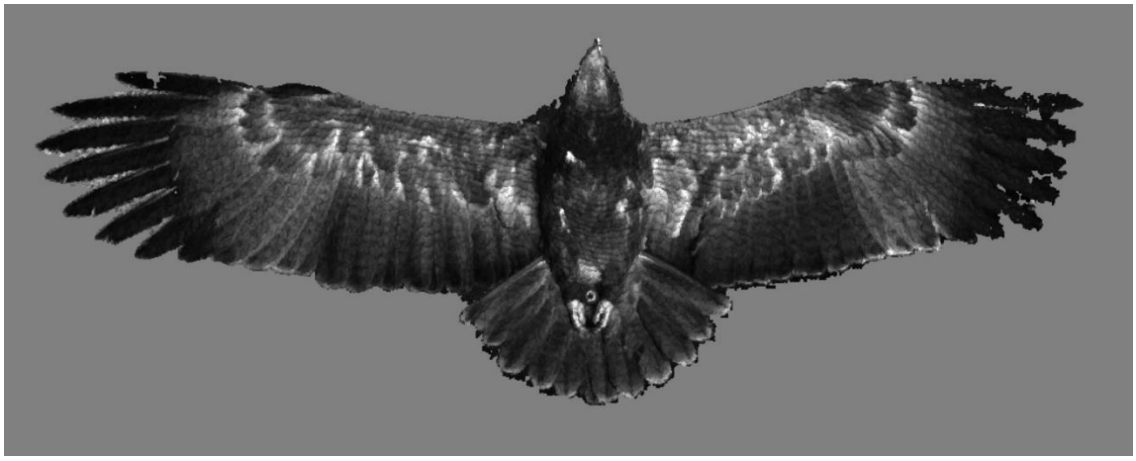

***Figure 7*** Ventral surface reconstruction of a Tawny Eagle gliding in ground effect. This reconstruction consists of approximately 360,000 points. Points are colour-coded based on sensor grayscale value.

### Ground effect

Flight heights were less than a semi-span above the ground, which placed the birds in moderate ground-effect. We analysed the response to ground-effect by separating the flight configurations into four categories: 1) body dynamics, consisting of speed, trajectory, and orientation of the body; 2) wing posture, consisting of rotations of the wing about the shoulder; and 3) wing surface, consisting of twist, camber, etc.; and 4) tail dynamics, consisting of spread angle, pitch, roll, and yaw.

The dynamics of these configurations can be determined by segmenting the point clouds into their respective anatomical regions (**Fig. 8**) and performing rigid transforms to align the segments both

within and among flights and flight treatments. We began our analysis on representative quasi-steady instances of each steady flight; however, relatively little morphing occurred in response to ground-effect, so we are delaying that analysis to emphasize the more dramatic wing morphing responses induced by gusts.

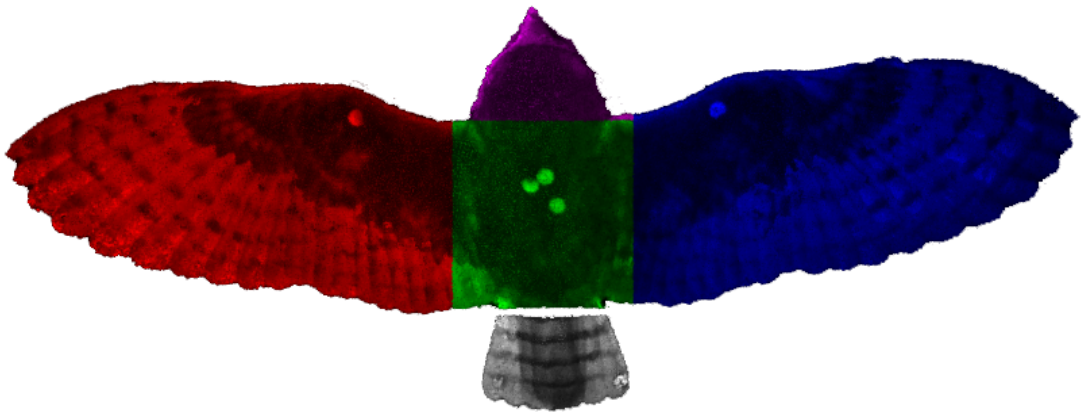

***Figure 8*** *Example of automatic segmentation of Barn Owl. Colour-intensities represent grey-scale values of disparity map. Left wing is red, right wing is blue, body is green, head is purple, and tail is grey.*

When encountering the increased quasi-static loading of ground effect, birds do not substantially modulate their wing surface, despite the numerous degrees of freedom available. The surface of each wing was similar across flights and treatments regardless of species. This similarity allowed us to map the wings onto one another through an *iterative closest point* algorithm operating on the perimeter of the point clouds. The wings required rotations in all three-axes to overlap, but the surface was remarkably consistent (**Fig. 9**). Analysis on the surface is ongoing, but preliminarily, it appears that gross shoulder rotations may be the dominant approach to handling the quasi-steady increased loading of ground-effect. The most obvious difference in wing shape due to ground-effect was reduced deflection of a single primary in the Tawny Owl, among multiple other modulations of aerodynamic parameters.

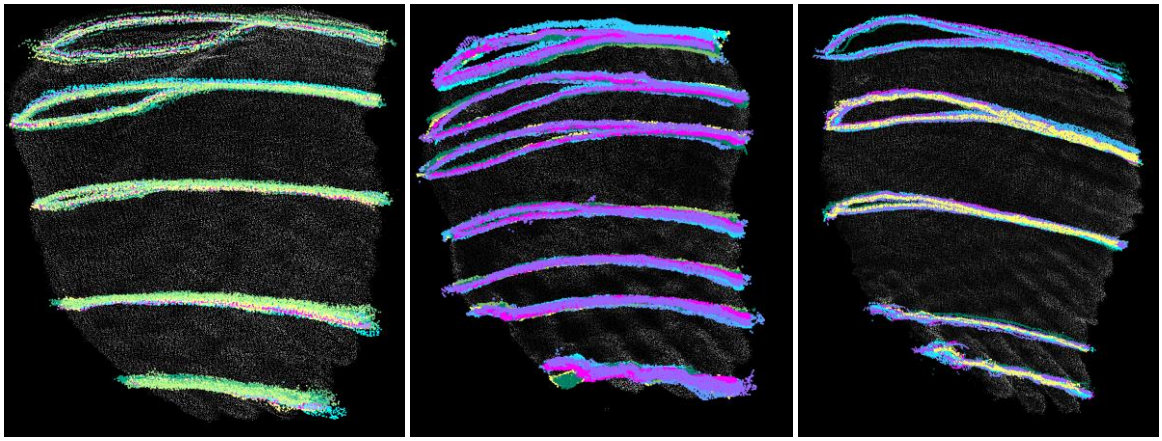

***Figure 9*** *Lateral, elevated view of aligned left wings of the Barn Owl (left), Tawny Owl (middle), and Northern Goshawk (right). Colours indicate different flights: warm colours are flights in ground-effect, and cool colours are control flights. The number of wing surfaces shown are (left-to-right): 13, 9, and 12.*

We decomposed the transforms for wing and body alignment into rotations approximating pitch, roll, and sweep. Modulating body and/or wing pitch orientation was the only consistent response among those gross movements to ground-effect lift enhancement. The Tawny Owl decreased both wing and body pitch in ground effect, while the Northern Goshawk decreased only body pitch (**Fig. 10**).

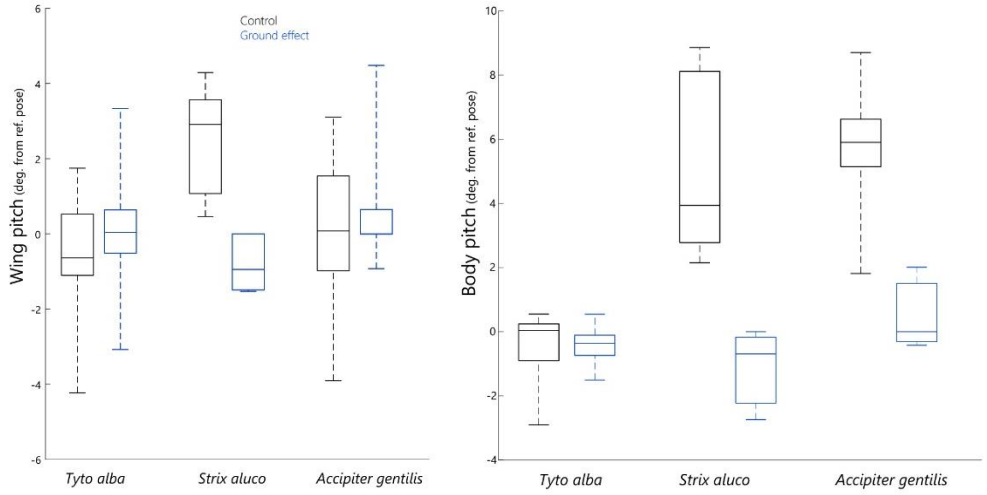


***Figure 10*** *Wing and body pitch for the Barn Owl (*Tyto alba*), Tawny Owl (*Strix aluco*), and Northern Goshawk (*Accipiter gentilis*).*

### Particle tracking velocimetry with neutrally-buoyant soap bubbles: CFD Validation

We validated our computational fluid dynamic models by comparing the wake and downwash to those from birds gliding through neutrally-buoyant soap bubbles. The lift estimated through CFD of the Barn Owl mesh accounts for 95.5% of body weight using the SST model assumptions of the flow. Alternative CFD models either produce comparable weight support; such as, k-ω, and Reynold's stress; or they produce ~5% more weight support; such as, k-ε and Spalart-Allmaras. Using the SST model, the estimated downwash behind the model matches the measured downwash both in magnitude and in covariance with span (Fig. 11). The agreement between

measurement and CFD for not only flow averaged weight support, but also downwash provides a well-validated model around this gliding condition.

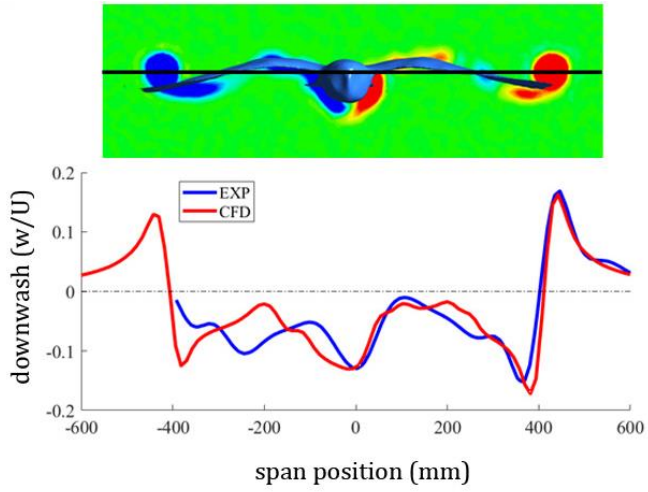


***Figure 11 Downwash validation for a gliding Barn Owl.*** *Top) vorticity in the transverse plane behind the mesh barn owl. Black line denotes section of downwash transect. Bottom) Normalised downwash at span locations. The CFD model (red) not only matches the measured (blue) magnitude, but also demonstrates similar covariance between downwash and span location.*

### CFD: Ground-effect

As birds fly near the ground, the aerodynamics changes as a response to the ground constraining the movement of the air. This ground effect modifies the pressure across the bird (Fig. 12), resulting in increased lift and decreased drag (Fig. 13). The reduction in lift and drag can be understood by changes to the relative flow.

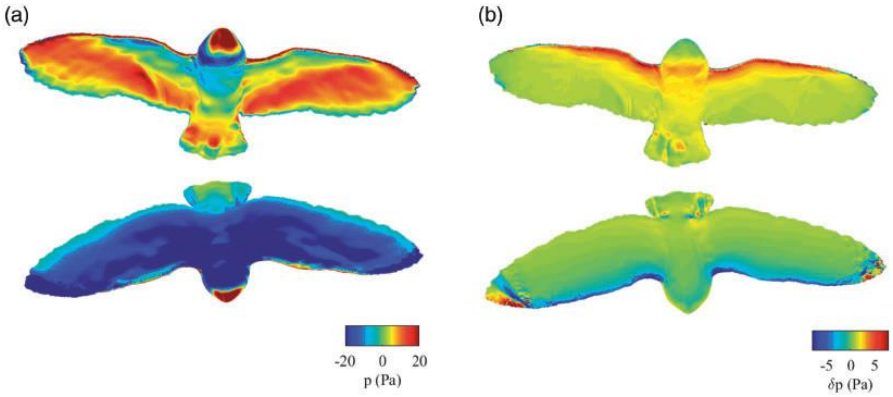


***Figure 12. Pressure distribution across the surface of a barn owl and its change in ground effect.*** *a) The pressure distribution across the barn owl far from the ground. b) The difference in pressure distribution far from and near to the ground (height/chord=1.17). Positive values indicate greater pressure in the ground-effect case.*

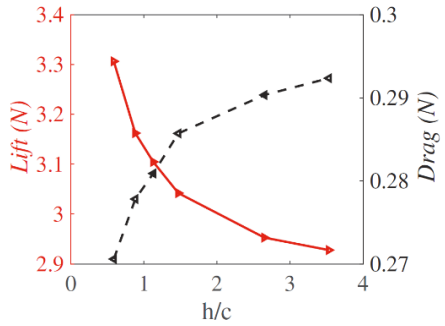


***Figure 13. Flying near the ground increased flight efficiency.*** *With increased proximity to the ground, lift (red) increased and drag (black) decreased.*

The changes to the flow can be estimated by considering the ground effect to be equivalent to a mirror-image bird, where the plane of reflection is at the ground. Using lifting line theory, we can replace the bird and its mirror image with lines vortices, and estimate the changes to the flow experienced by the bird that result from the mirror image. The mirror-image bird produces lower relative forward flow speeds and greater upwash (Fig 14), which helps to explain the reduced drag and increased lift.

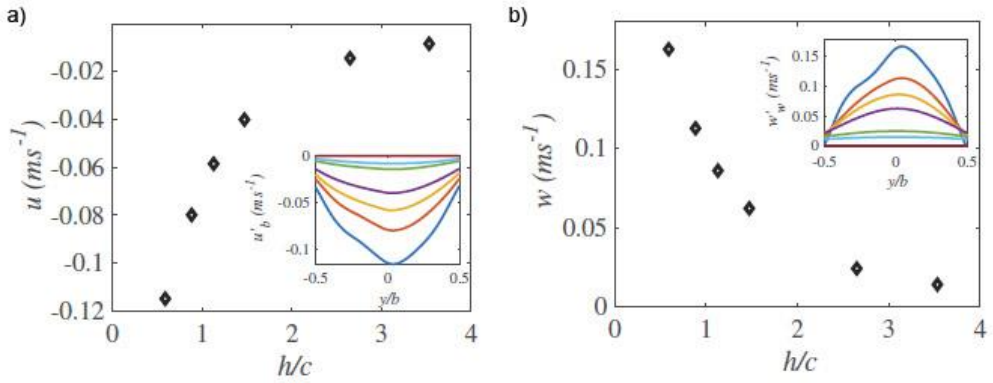


***Figure 14. Changes in the flow induced by mirror-image vortices approximating ground effect.*** *a) Forward speed, u, decreases, and upward flow, w, increases, with increasing proximity to the ground. a-b) Insets depict local changes in flow across the span.*

### Mass distribution

With our collaborators at the University of Bristol, we determined mass distribution of three deceased Barn Owls from µCT scans at the RVC's imaging suite. The mass distribution provides insight into gust rejection mechanisms (discussed below), and into centre of mass of the gliding Barn Owl.

### Vertical gust rejection

All birds studied effectively rejected the vertical gust. The Barn Owl, the bird with the lowest wing loading in our study, showed the most dramatic morphing. As we increased the flow speed in increments, we observed a dose-dependent response in kinematics (fig. 15a). However, the movement of the body in response to the gust was not clearly dose-dependent, the gust impulse applied to the Barn Owl was much less than predicted by simulation (fig. 15b). Two of the largest

kinematic responses were wing elevation and wing pitch, and we observed elevation occur consistently prior to wing pitching (Fig 15c,d).

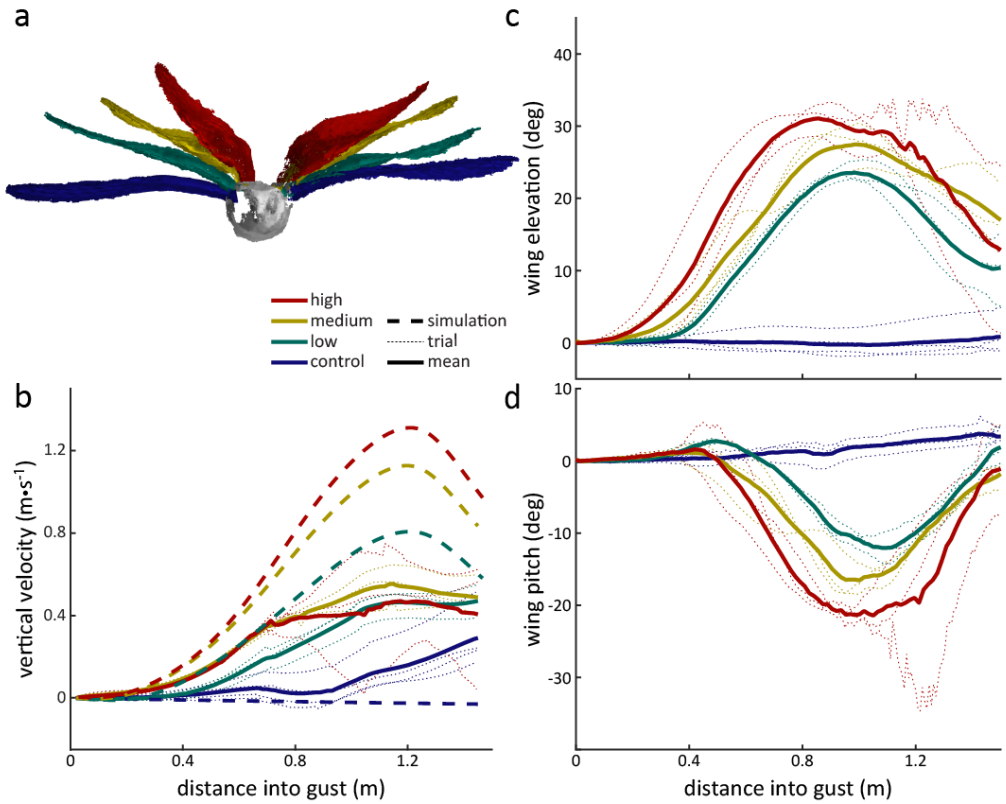


***Figure 15. The bird rejected the vertical gust with large dose-dependent rotations about the shoulder.*** *a) 3D reconstructions of the bird 90% through the gust perturbation, wings colour-coded by gust intensity. b) Vertical velocity of the centre of mass of the bird's torso (solid lines-mean response) was perturbed less than the CFD simulation (dashed) predicted. c) Wings elevated about the shoulder in dose-dependent response to gust intensity. d) Wings pitched downward after increase in wing elevation.*

We considered two independent mechanisms for gust rejection in birds, 1) an inertial mechanism, whereby the relative motion of the mass of the wings (11% body mass) reduces the motion of the torso and head; and 2) broad aerodynamic mechanisms based on changes in the orientation and shape of the wings; such as decreasing the wings' angle of attack, which reduces the lift generated. We quantified the magnitude of these two gust rejection mechanisms using mass-normalized impulse, and by calculating the deviations between 1) the torso and the whole bird centre of mass; and 2) the whole bird centre of mass and the rigid body CFD-based simulation. Further, we estimate the significance of the rejection mechanisms by normalising by the potential applied gust impulse, calculated as the deviation between rigid body simulations with and without gust (Fig 16a).

Due to conservation of momentum, the relative upward motion of the mass of the wings (19% total mass) pushed the torso downwards relative to the centre of mass of the whole bird. This inertial effect reduced the impulse to the torso and head (Fig 16b), rejecting at the point of peak wing

velocity 33 ± 5% (mean ± s.e.m.) of the total expected gust impulse. At the same instant, there was negligible aerodynamic rejection, with the whole bird centre of mass velocity closely following that of the simulation of the rigid CFD model, with an estimated aerodynamic rejection of only 6 ± 6% (Fig. 16c). Later, when the wing pitched downward, there was an increase in the deviation between the measured vertical velocity of the whole bird centre of mass and the rigid body simulation (Fig 16c), indicating large aerodynamic-based gust rejection. The combination of these two mechanisms acted to reduce the effect of the gust on different time scales, with the faster inertial mechanism acting to reduce the initial effect of the gust on the torso and head, before slower aerodynamic mechanisms started to act to reduce the effect on the whole bird (Fig 16d).

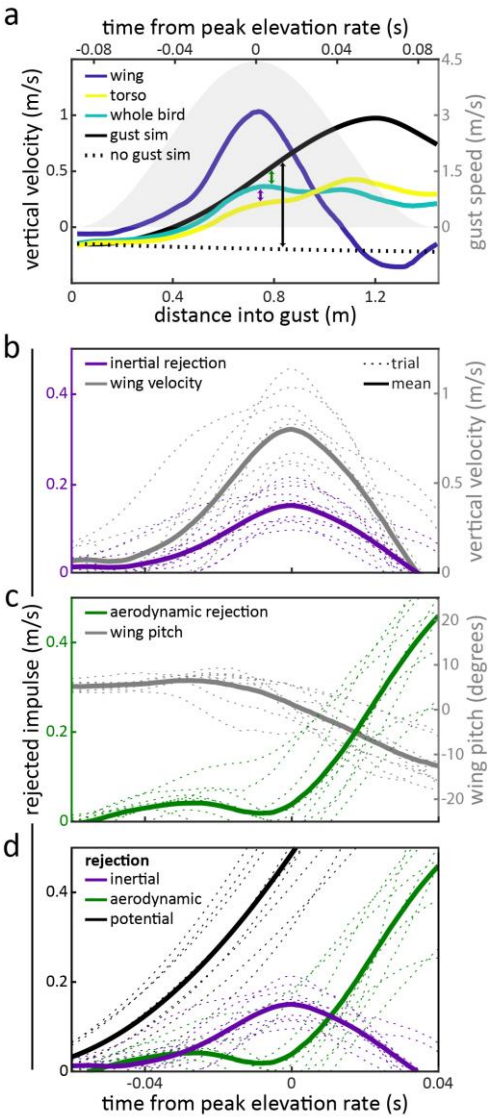


***Figure 16. Inertial mechanisms reject gust impulse applied to the torso before aerodynamic mechanisms take effect.*** *a) Representative medium-intensity gust trial displaying centre of mass vertical velocity of wing, torso, whole bird, and rigid simulations with and without gust. Vertical arrows in centre of plot indicate how differences in paired parameters determine rejection terms in (b-d; coded by colour). b-d) Rejected gust impulse (left y-axis) versus time from peak elevation rate, and kinematic correlates (right y-axis). b) Vertical wing velocity (grey) coincided with increasing rejection of the gust impulse by means of inertial mechanisms (purple). c) Aerodynamic rejection mechanisms (green) remained at low levels until shortly past peak elevation rate (t=0), then increased coinciding with downward wing pitch (grey). d) Inertial mechanisms (purple) rejected on average 33% of the gust impulse applied (black, calculated from simulation) prior to aerodynamic mechanisms (green) initiating. b-d) Trials from all gust intensities (excluding controls) are shown as dashed lines, solid lines are mean response.*

The explanation for the inertial rejection mechanism, and its tuning, are related to a concept known as the centre of percussion, which depends on the mass and force distributions across the wing. For any object that pivots about a freely translating point, like the wing pivots about the shoulder of a flying bird, there exists a point on the object, the centre of percussion, where force applied will not accelerate the pivot, but will rotate the object (Fig 17a). This is similar to the 'sweet spot' in bat and racquet sports, where the reaction force experienced at the hand due to hitting the ball is reduced to zero if struck at a particular spot on the bat: this spot is the centre of percussion. As a test of this inertial mechanism hypothesis, we examined whether the centre of percussion of the wing coincided with the centre of pressure during steady gliding. Based on density calibrated x-ray computer tomography (CT) data for a similarly sized specimen of the same species, the centre of percussion of the wing was located just inboard (2.6 cm, or 5.9% semi-span) of the centre of pressure calculated using the CFD model (Fig 17b). This means that changes in the lift force on the wing would mostly have resulted in rotation of the wing about the shoulder with only a small upward acceleration of the torso. The magnitude of torso acceleration is determined by the mechanical properties of the shoulder joint, with increasing shoulder joint stiffness shifting the point where a perturbation would produce no change in torso acceleration further outboard. Birds may then be able to tune the dynamics involved with gust rejection by modifying the stiffness of their shoulder joint through muscle activity, potentially utilizing a more compliant shoulder for atmospheric turbulence rejection (conferring straighter trajectories) and increasing shoulder stiffness for atmospheric energy harvesting.

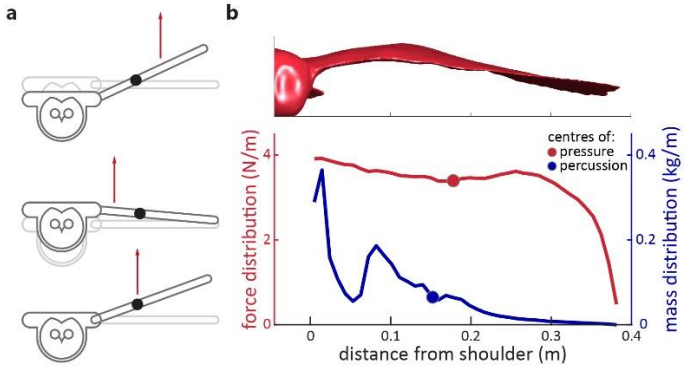


***Figure 17*** *Aerodynamic force acting at the centre of percussion of the wing will produce a rotation about the shoulder with no vertical displacement. a) A force acting outboard of the centre of percussion (top) will rotate the wing and displace the torso down, a force inboard (middle) will rotate the wing and displace the torso upward, while a force at the centre of percussion (bottom) will only rotate the wing. b) Mass distribution of the wing showing the centre of percussion (assuming a free shoulder pivot) and the aerodynamic centre of pressure during steady gliding flight from CFD simulations.*

### Mechanics of gust rejection

The mechanics of centre of percussion for a bird or hinged-wing aircraft are complex, but with simplification, the equations of motion are tractable and provide intuitive sense. The centre of percussion is the point on a "hinged object" where an external force acting on the point causes the "object" to move, without applying a net force to the hinge. To make an analogy with birds, the hinged object is the wing, and the hinge is the shoulder connected to the body; through stabilising the hinge, we stabilise the body. Where this analogy requires additional complexity is that the wing is not a free hinge, the wing(s) support body weight through muscular torque at the shoulder.

Therefore, minimizing accelerations of the shoulder/body requires consideration of both the applied aerodynamic force and the shoulder torque.

We derived the equations of motion for a steady gliding bird that experiences either 1) small changes in aerodynamic force, location of the force, and shoulder torque; or 2) a super-imposed force/torque on the wing. The first derivation is relative to the resting torques at the shoulder, and provides insights from the perspective of the shoulder actuation system, the second derivation is relative to the imparted change in force caused by the gust, which if known is more easily modelled. Key elements of the derivation are below:

$m_w$ – wing mass
$m_b$ – body mass
$a_w$ – wing acceleration
$a_b$ – body acceleration
$r_w$ – distance from shoulder to centre of **mass of the wing**
$r_a$ – distance from shoulder to centre of **pressure**
$r_p$ – distance from shoulder to centre of **percussion**
$F_a$ – aerodynamic force acting on one wing
$F_b$ – force on the body
T – torque at shoulder (spring, damper, actuator, etc.)
I – moment of inertia of the wing (about elevation axis, located at centre of mass)
ë – wing elevation (rotational) acceleration

Relationship between centre of percussion and moment of inertia
$I = r_w m_w (r_p - r_w)$

The relevant forces in the system are
$F_a$ the aerodynamic force
$F_{shear}$ the shearing force at the shoulder between the body and wing
T the torque produced at the shoulder

In trim, torque balance at the shoulder, force balance, and force applied by wing to body
$m_w (r_p - r_w)( a_w - a_b) = F_a (r_a - r_w) - F_{shear} r_w – T$
$½ m_b + m_w = F_a$
$F_{shear} = -½ F_b$

Below is derivation 1)

Change in torque balance after a change in lift and change in position of centre of lift (additionally with force replacing acceleration terms)
$(dF_w - dF_b m_w/m_b) (r_p - r_w) = F_a(dr_a) + dF_a(r_a - r_w + dr_a) - dF_{shear} r_w – dT$

Tidying algebra
$½dF_b [2*r_w - r_p + 2*m_w/m_b (r_w - r_p)] = F_a (dr_a) + dF_a(r_a - r_p + dr_a) – dT$

If we make: $c = r_w [1 - I/m_w r_w^2 (1 + 2*m_w/m_b)]$
then body acceleration is more simply related to torque:
$½\ c\ dF_b = F_a (dr_a) + dF_a(r_a - r_p + dr_a) - dT$

Assuming the gust applies no acceleration at the shoulder/body, what are the changes in torque, aerodynamic force, and the point of force application?
$o = F_a (dr_a) + dF_a(r_a - r_p + dr_a) - dT$
Or
$dT = F_a (dr_a) + dF_a(r_a - r_p + dr_a)$

We can then derive non-dimensional forms of the equation for gust rejection:

| | |
|---|---|
| $T^* = dT / T = dT / (F_a r_a)$ | % increase in force from steady glide |
| $F^* = dF / F_a$ | % increase in torque from steady glide |
| $o^* = (r_a - r_p)/ r_b$ | Difference in centres of pressure & percussion per span |
| $dr^* = dr / r_b$ | % change in wing force location |

$a\ T^* = dr^* (1 + F^*) + F^*(o^*)$

Derivation 2 is similar, except instead of modifying the original force and position, a new torque term is added.

Replacing: $F_a(dr_a) + dF_a(r_a + dr_a - r_w)$

with: $F_{add}\ r_{add}$

and solving, produces:

$dT/F_{add} = r_{add} - r_p$

& with nondimensional units:

| | |
|---|---|
| $\check{T} = dT / F_{add} / r_{add}$ | % torque relative to the torque from the superimposed gust |
| $r_p^* = r_p / r_{add}$ | centre of percussion relative to gust position |

$\check{T} = 1 - r_p^*$

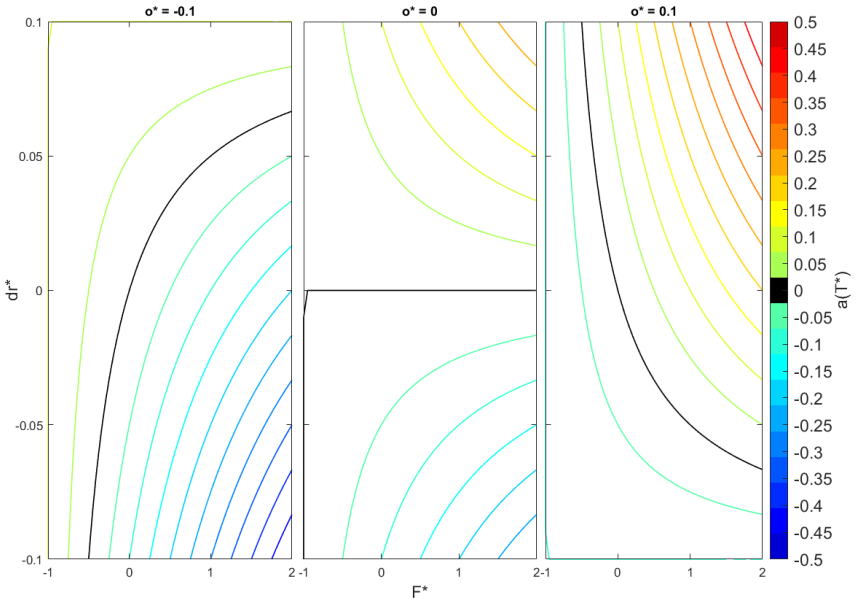


***Figure 18 Rejecting gusts through shoulder torque.*** *If the same shoulder torque actuators must also support body weight, then considering the torque relative to body weight can provide helpful bounds to the problem. Above are three plots for centre of pressure's position relative to centre of percussion: inboard, at, and outboard.*

From these equations, we can understand how torques at the shoulder must change in order to reject gusts of varying position, magnitude, or both. Changes in torque could be active and/or passive, and both may be beneficial. For simplicity, we discuss changes in torque abstractly and do not consider the cause of change in torque.

If gust position changes without changing magnitude, then the necessary torque to reject the gust is equal to the torque produced by an infinitely stiff hinge. In no other scenario can infinitely stiff hinges reject a gust, these wings produce excess shoulder torque equal to the position of the centre of percussion scaled by the change in force ($r_p * dF_{a)}$ resulting in upward body acceleration. In contrast, a wing on an infinitely compliant hinge but still capable of supporting body weight, can reject a gust if the gust's centre of pressure shifts towards the centre of percussion (Fig. 18). These results demonstrate that a compliant wing hinge is generally beneficial, and that through tuning mass distribution and shoulder torque a wide range of gusts are rejectable through these mechanics analogous to an active suspension system.

**Computational modelling: gust-rejection interactions**

The lift curve of the wing plays a substantial role in enhancing inertial gust rejection. Simulating the centre of percussion effects on gust rejection over time shows that soft stall helps to maintain alignment between the centres of pressure and percussion throughout an upward gust. At Reynolds numbers of ~$10^6$, soft stall phenomena are relatively common. Additionally, the compliance of biological wings tends to lead to shallower lift curves than expected from rigid wings. The simulated lift curve for the barn owl was relatively insensitive to angle of attack once the lift coefficient exceeded 0.8. When we simulate a wing with a lift coefficient that does not exceed 1 (Fig. 19a), gust rejection is nearly perfect with a compliant shoulder hinge (Fig. 19e). Despite the flow gradients across the wing induced by the rapid wing movement, they lead to negligible changes in the

spanwise force distribution (Fig. 19b). When the lift curve is not flat, the centre of pressure moves rapidly away from the centre of percussion, and performance is then dominated by aerodynamic rejection (Fig. 19e). Thus, the two effects are complimentary, when the lift-curve is steep aerodynamic rejection is substantial, when the lift-curve becomes shallower inertial rejection can supplement the effect.

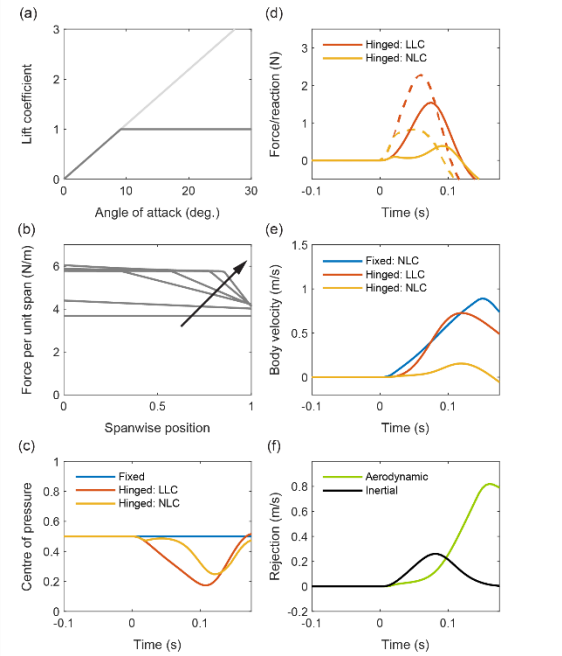


***Figure 19 Dynamics of a simulated hinged-wing and fixed-wing aircraft in a strong upwards gust ($v_{gA} = 0.625U$) with either a linear (LLC) or nonlinear lift curve (NLC).*** *(a) Lift curves for the LLC (light grey) and NLC (dark grey) aircraft. (b) Spanwise force distributions at six evenly spaced time points between gust onset and peak velocity ($t = L_g/2U = 0.0875$ ms) for the hinged-wing aircraft with NLC. The arrow identifies forward chronology. (c) Normalised centre of pressure $l_F/b$ for the hinged and fixed systems with LLC or NLC, as indicated. For the fixed system, $l_F/b = 0.5$ regardless of the lift curve. (d) The reaction on each wing (dashed lines) or on the body (solid lines). (e) Vertical body velocity of the fixed and hinged systems with LLC or NLC, as indicated. (f) Rejection terms for the hinged-wing aircraft with NLC.*

### Gust-rejection in a bio-inspired glider

To test the effectiveness of the inertial gust-rejection mechanism, we implemented it in a glider. The glider possessed a Z-hinge, which allowed the wings to elevate and depress about the hinge. The lift produced by the wings supported the body by transmitting the force through elastic tensioners that hold the wing in a level configuration (Fig. 20). In this configuration, the glider should be able to reject gusts vertically upward or downward. Finally, we added mass to the wings to align the centres of percussion and pressure.

The hinged-wing glider flew through upward and downwards gusts of peak speed equal to 95% of the glider's forward speed. The hinge mechanism allowed the glider to reject a significant fraction of the gust. For the upward gust, at the instant of peak inertial rejection, the glider rejected 40% of the impulse induced by the gust: 23% by wing inertia and 17% by changes in external aerodynamic force. For the downward gust, at the instant of peak inertial rejection, the glider rejected 27% of the impulse induced by the gust: 21% by wing inertia and 6% by changes in external aerodynamic force

(Fig. 21). As in the bird, and in the simulation, inertial rejection was sizeably more than aerodynamic rejection.

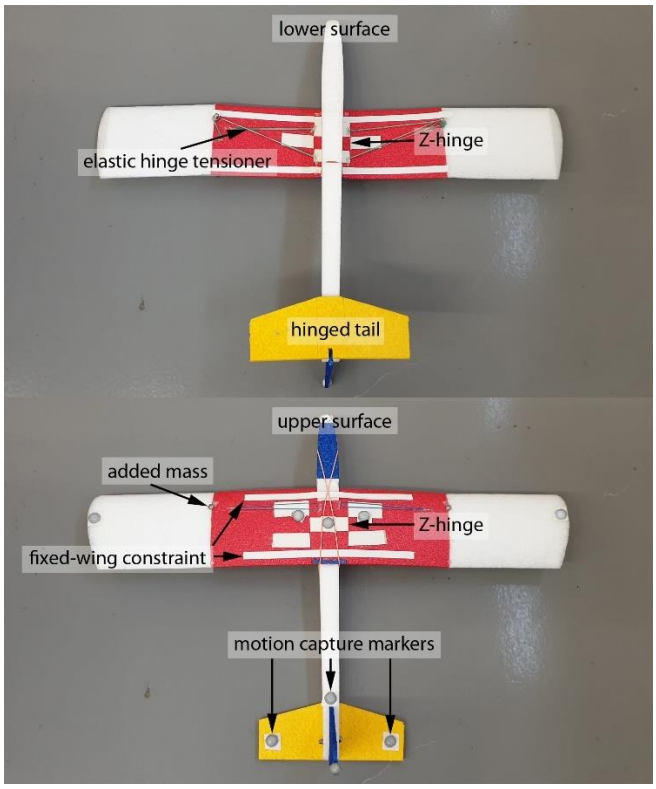


***Figure 20 The upper and lower surfaces of a glider with bio-inspired gust rejection mechanism.*** *Elastic hinge tensioners allow for weight support, added mass adjust centre of percussion to be in closer alignment with centre of pressure, motion capture markers were used to analyse rejection response and estimate the dynamics of the centres of mass of the wings, fuselage, and whole aircraft.*

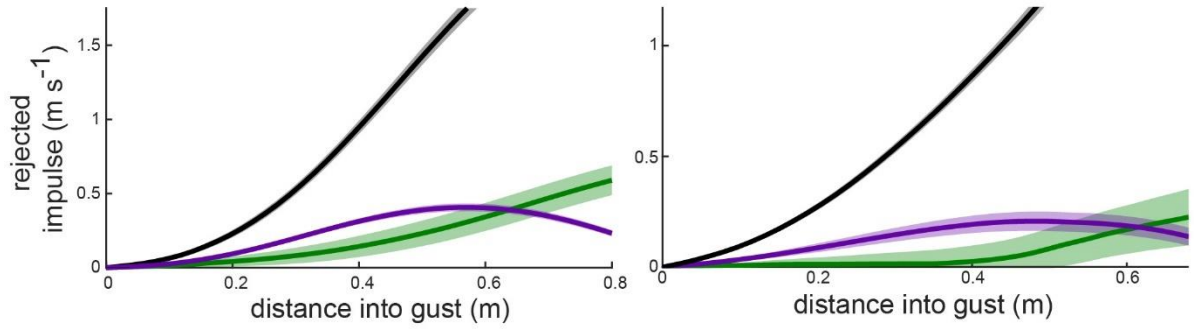


***Figure 21 Glider's gust rejection of upward (left) and downward (right) gusts of speed equal to 95% of glider's forward speed.*** *Inertial (purple) and aerodynamic (green) rejection exhibit similar patterns in time as seen in the owl and the simulated dynamics of a glider with nonlinear lift curve. Inertial rejection initially dominates, and aerodynamic rejection lags behind.*

**Particle tracking velocimetry with neutrally-buoyant soap bubbles: comparison with aircraft**

***Figure 22 Wake visualization behind three birds demonstrates excess downwash behind the tail.*** *Left) Multi-strobe-exposure photographs capture the wake behind a Barn Owl, Tawny Owl, and Northern Goshawk; top to bottom respectively. Right) Reconstructed wake of the Tawny Owl using Q-criterion to demonstrate the strong downwash induced behind the body and tail.*

Trailing vortices follow the tail, and their associated downwash near the bird centreline, demonstrate that the body/tail section produces greater aerodynamic lift per span than the wings (Fig 22). This positive lift is opposite to that required for tails producing stability through longitudinal dihedral: the tails of conventional, passively stable aircraft produce negative lift and accelerate air in the opposite direction – upwards – which would be associated with trailing vortices of the opposite sense.

If not used for passive pitch stability, it might be expected that the bird tails are necessary for weight support during slow flight. However, the observed trailing vortices behind the tail indicate that lift contribution of the central section is considerably in excess of simply filling in the lift distribution between the wings. The lift coefficients calculated for the Tawny Owl and Goshawk were high for raptor wings (Withers, 1981; Van Oorschot et al., 2016), close to 1, so there is the possibility that tail lift is merely allowing slow gliding while preventing stall, analogous to the flaps deployed by landing aircraft (Pennycuick, 1975). However, the Barn Owl operated with a mean lift coefficient close to 0.7 – well below the maximum lift coefficients measured for isolated raptor wings (Withers, 1981; Van Oorschot et al., 2016) – yet also displayed the step increase in downwash behind the tail, meaning that a simple account based on stall avoidance is insufficient.

The apparently excessive aerodynamic lift produced by the body/tail is significant because it affects the drag experienced by the gliding bird. To understand its implications in terms of overall drag, we adapt classical approaches (Tucker, 1987; Spedding and McArthur, 2010) to model the drag as the sum of three components:

$$D = \left(\frac{C_L^2}{\pi \,\mathrm{AR}\, e_i} + \frac{k C_L^2}{e_v} + C_{D0}\right)\frac{\rho}{2} S V^2$$

The first term is the inviscid or induced drag coefficient – that associated with accelerating air downward in order to provide weight support. The second and third terms together combine to give the profile drag coefficient, with $C_{D,0}$ the minimum drag coefficient (assumed here to occur close to zero lift). It is important to highlight that the second term increases with the square of lift coefficient, denoting the C-shape of a lift-drag polar for a generic pre-stall aerofoil (2-D); the curvature of the polar relates to the constant *k* that expresses the quadratic rise of this drag term with lift (Spedding and McArthur, 2010), and tends to be more extreme at lower Reynolds numbers (Abbott and Doenhoff, 1949). This dependency on lift can present some confusion as it is sometimes convenient to combine it with the inviscid induced drag term (Houghton et al., 2016; Spedding and McArthur, 2010), which also varies with $C_L^2$. It is, however, a form of viscous drag and is therefore of proportionally greater magnitude at lower Reynolds numbers.

Inviscid or induced drag is classically minimized with an elliptical lift distribution across the span (Prandtl, 1921; Munk, 1923), (Fig. 17a, green lines) leading to constant downwash velocity of sufficient magnitude to support body weight, but resulting in lift coefficients that vary across the planform (green lines Fig. 17c). Viscous, profile drag, in contrast, is minimized (relating to red lines, Fig. 17) if lift coefficient is constant for every section, as, from **Error! Reference source not found.**

$$e_v = \frac{C_L^2}{\overline{C_l^2}} \qquad (0)$$

for wings of sectional lift coefficient $C_l$ and near-constant aerofoil section shape. This requires that lift is evenly distributed across the planform *area*, and so spanwise lift profile matches the aerodynamic chord profile – in which case $\overline{C_l^2} = C_L^2$ and $e_v$=1. Minimization of inviscid, induced drag and viscous, profile drag cannot both be met simultaneously without an elliptical planform.

Downwash velocity fields for each trial were measured for a transverse plane close after the passage of the tail trailing edge, but also dependent on good bubble seeding coverage. As these planes were not exactly at the 'lifting line' aerodynamic abstraction (a concept underlying the simplest three-dimensional wing theory – Prandtl, 1921; see Abbott and Doenhoff, 1949), downward convection, though gradual (Fig. 22), meant that no single horizontal transect across the plane provided an adequate measurement of downwash profile; instead, we show the range between maximum and minimum downwash values for transects at 0 mm, 50 mm and 100 mm below the wingtips (Fig. 23c).

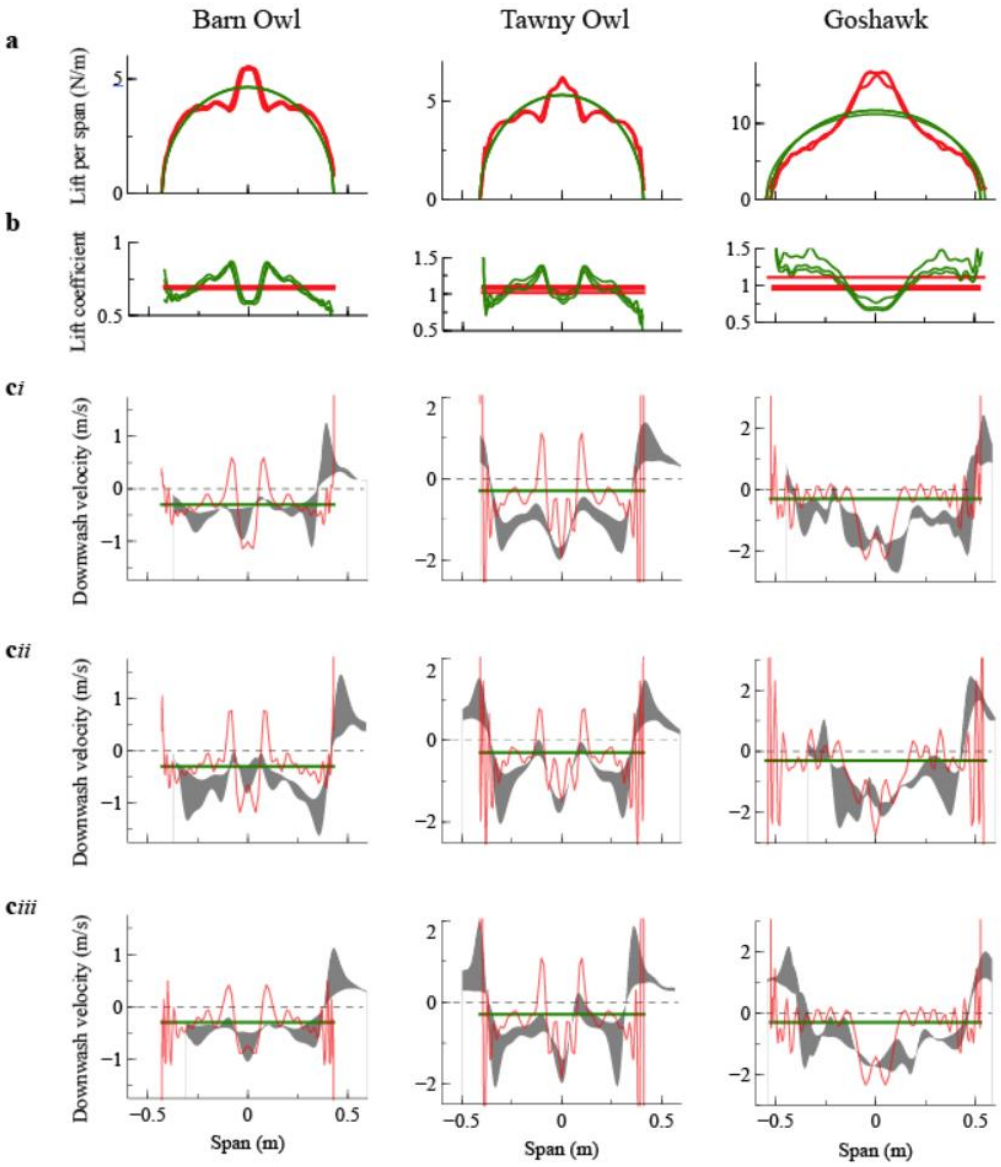


***Figure 23 Comparisons of competing models of drag minimization.*** *Hypothetical spanwise lift profiles (a) and associated sectional lift coefficients (b), and their modelled consequences in terms of downwash profiles (coloured lines (c) for three glides per species (i-iii)). Green lines indicate the hypothetical inviscid or induced-drag minimizing case, with elliptical spanwise lift distribution, variable lift coefficient and constant downwash velocity across the span. Red lines indicate the theoretical viscous or profile-drag minimizing strategy, with lift distribution matching chord profile of wings/body planform resulting in constant spanwise lift coefficient and – because the planform is not elliptical – varying downwash velocities. The deviation in planform from elliptical, largely due to the projecting central tail area, is evident from (A), in which the loading profile is either elliptical or in direct proportion to chord (excluding the head). Grey shadings indicate measurements spanning the maximum to minimum downwash velocities across horizontal transects of transverse planes after passage of the bird, located level with the wingtips, 50mm and 100mm below the wingtips.*

Downwash values at the centreline do not match the prediction of constant downwash from inviscid induced drag minimization. Instead, they provide a good quantitative match (Fig. 23) with predictions based on constant spanwise lift coefficient and minimized profile drag. The success of the second model, and contrast with aircraft-based postulations, may reflect both: the relatively large contribution of viscous effects at the low Reynolds numbers ($\sim$100,000) experienced by birds; and a low cost to birds for their moderate deviation from perfect induced drag minimization. Indeed, using the constant-$C_L$ theoretical downwash profiles, $e_i$ is only reduced to 0.8-0.9.

**Morphing the tail to reduce drag**

We observed variation in tail configuration among the barn owl's steady glides, with tail pitch angle ranging from 18-35 degrees and spread angle ranging from 7 to 33 degrees. We explored the effects of these tail postures by modifying our CFD mesh using basic geometric transforms to appear as similar configurations in order to explore the role of tail pitch and spread on lift and drag.

If angle of attack is maintained and lift is allowed to exceed that necessary for body weight support, increasing tail pitch and spread both lead to greater lift and drag (Fig. 24). However, if the angle of attack is reduced, i.e., the whole bird geometry is pitched, until lift supports body weight then within there exists an optimal tail configuration for minimising drag (Fig. 25). When maintaining body weight support, the barn owl configures its tail to achieve minimum drag (Fig. 25,a). The Barn owl could produce substantially more lift with its tail than it does, which suggests that the tail's role is not just to aid in slow flight, but to aid in slow efficient flight.

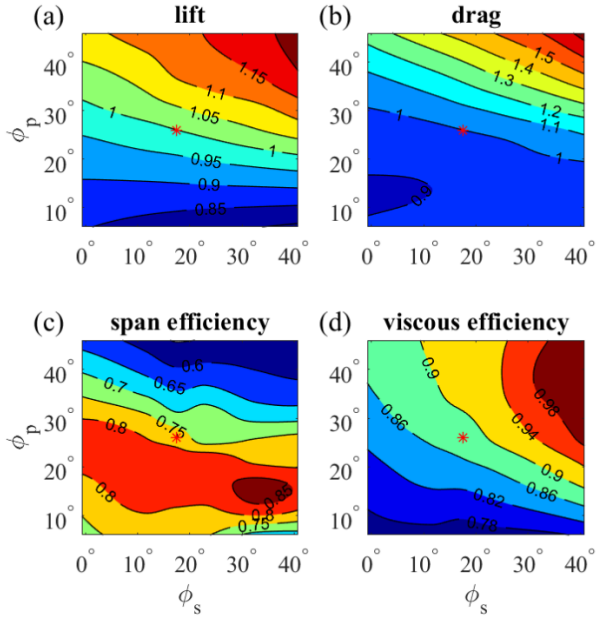


***Figure 24 The effect of tail configuration on lift, drag, and flight efficiencies.*** *When allowing lift to exceed body weight support, with increasing tail pitch and span: (a) lift and (b) drag increases. (c,d) Greatest efficiency typically occurs with a spread tail, but optimal span efficiency occurs with only a small pitch to the tail, while optimal viscous efficiency requires substantial tail pitch.*

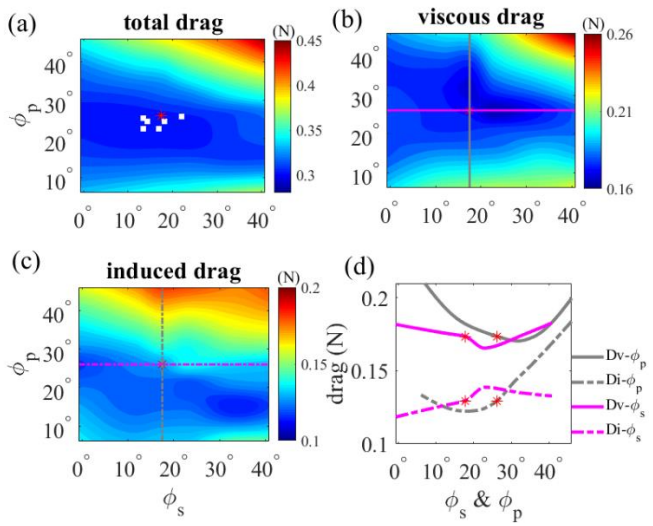


***Figure 25. When weight support is maintained, there is an optimal tail configuration for minimising drag.*** *(a) Total drag is at its minimum at moderate tail spread and pitch angles. White dots (and red asterisk) indicate observed configurations of the tail. b-c) Separating drag into its viscous and inviscid/induced components, shows that the adopted configurations represent a balance of minimising both drags, and is not perfectly optimal for either one. Further, both cannot be optimised with the same configuration. d) Cross-sections through viscous and induced drag showing the effect on drag of changing only pitch or spread. a-d) Red asterisk, indicates the tail configuration used in the flight that serves as the foundational CFD geometry.*

## Morphing with speed

We examined how the barn owl, tawny owl, and northern goshawk changed wing shape and/or pose when gliding across a range of self-selected speeds. We analysed wing shape by correcting for postural changes (rigid-body transforms) of the wings and aligned them using the surface data. Below we describe the average configuration and its changes with speed.

*Average configuration*

*Body posture*

Each of the three birds oriented their body-coordinate system in a differently relative to the flow. All flew with a nose-up configuration (pitch: -4.5 ± 0.4°, -11.6 ± 1.4°, -11.9 ± 2.0°; mean ± s.e.m.). The body was not held a constant yaw relative to the flow, the standard deviation of yaw was 2.0°, 4.6°, and 2.9°, and each bird's coordinate system was yawed relative the flow by 3.6 ± 0.6°, -2.8 ± 1.2°, 3.7 ± 0.8° (mean ± s.e.m.). Body roll, computed from asymmetry in wing elevation, was -0.2 ± 0.7°, 3.1 ± 1.2°, -6.5 ± 1.3° (mean ± s.e.m.).

*Tail posture*

For all birds, the average tail configuration was with tail feathers spread and held in a pitched configuration resulting in a depressed trailing edge. Pitch angle of the tail relative to the body-coordinate system was 18.7 ± 0.6°, 27.9 ± 1.4°, 23.5 ± 1.9° (mean ± s.e.m.). The spread angle of the feathers covered an arc of 35.8 ± 2.7°, 51.2 ± 2.6°, 90.7 ± 5.9°; well above the minimum observed arcs of 20.7°, 30.8°, 38.9°.

The size of the tail represented a relatively small fraction of the projected area in the two owls, T. alba and S. aluco, and a larger portion for the hawk, *A. gentilis*. The tail accounted for 8.2 ± 0.2%,

11.6 ± 0.3%, and 25.1 ± 0.7% of the planform area. As the tail was often held at steep angles relative to the planform, the tail would account for a greater fraction if it was held flat. Artificially rotating the tail to be coplanar with the planform, slightly increased the area represented by the tail to 8.5 ± 0.2%, 13.2 ± 0.3%, and 26.9 ± 0.9% of this artificial planform area, for T. alba, S. aluco, and A. genitilis, respectively.

*Wing posture*

We describe wing posture relative to a reference posture, where the plane of the wing is orthogonal to the dorsoventral axis, and swept about that axis into the average swept posture for each bird. The sign convention for describing the angle of the wings is based on the left wing (Fig. 26), and movements of the right wing were adjusted to describe the same relative motion as the left wing. Average wing posture is the average of both the left and right wings across all flights.

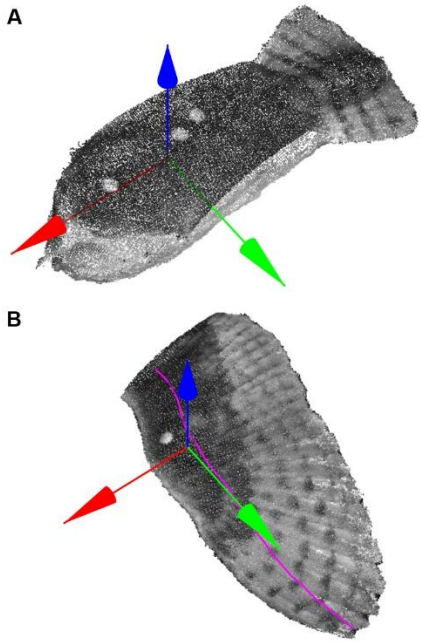


***Figure 26. Coordinate-system used to describe rotations of the body and wing in* T. alba *(representative).***

For the three birds, average wing posture placed the wings in a configuration leading to the wing tips being depressed and in anhedral, with the wing pitched resulting in the leading edge rotating upward. Finally, wing sweep computed on the quarter-chord line resulted in the wings being forward swept to varying degrees. The average elevation of the wings about the long axis of the body was -7.1 ± 1.0°, -12.5 ± 0.6°, -6.5 ± 0.6° (mean ± s.e.m.). The pitch of the wing was -1.3 ± 0.3°, -6.0 ± 0.5°, -8.4 ± 0.9°, resulting in increased angle of attack relative to the reference pose. By definition of our reference pose, mean wing sweep for each bird was approximately 0° (± 0.5°, ± 0.4°, ± 0.8°), but to compare birds we describe the sweep of the quarter-chord line through each chord: the best fit line through quarter-chord sections led to the wing being forward-swept -4.5 ± 0.2°, -7.9 ± 0.4°, -0.8 ± 0.2°.

*Spanwise distributions of the wing: the quarter-chord line, chord length, and twist*

Along the wing span, chordwise sections of the wing are nonuniform both in profile, but also orientation, size, and in position relative to adjacent sections (Fig. 27). The wings of all three birds twist over a range of 13.3 ± 1.3°, 19.1 ± 2.0°, 17.0 ± 1.5°, with the change in pitch most extreme distally, resulting in increased angle of attack with increasing span position, a type of wing design referred to as aerodynamic wash in. The chord length for all three birds decreases with increasing

span position, but wing taper varies by species. Notably, the goshawk's chord length begins to taper at approximately 40% semispan, and despite the bird's larger size, by approximately 70% semispan, chord length is shorter than that of *S. aluco*.

The protracting and retracting movement of the quarter-chord line follows a similar path near the root and at the wing tips for the two owls (*T. alba* and *S. aluco*), but the quarter-chord line protracts further forward in *S. aluco* over 20-95% of the semispan; by 75% semispan, the quarter-chord line is protracted forward nearly 50% further relative to that of *T. alba*. By contrast, the quarter-chord line of *A. gentilis* remains much nearer to that of the root.

While the wing-coordinate system attempts to make the wing surface flat, minimising the average displacement of all markers from the plane, because the wing is large proximally and tapered distally, the proximal wing is flatter than the distal region due to the area weighting. As a result, the quarter-chord line is not flat, and for each of the three birds tends to rise with increasing span. All three birds have proximal concave-down curvature and distal concave-up curvature. In *T. alba*, the concave-down curvature is strong, while the concave-up curvature is relatively gentle. The curvature of the quarter-chord line in *S. aluco* is rather moderate for both regions; and in *A. gentilis* the intensity of the curvature is the opposite of that in *T. alba*, gentle proximally and strong distally.

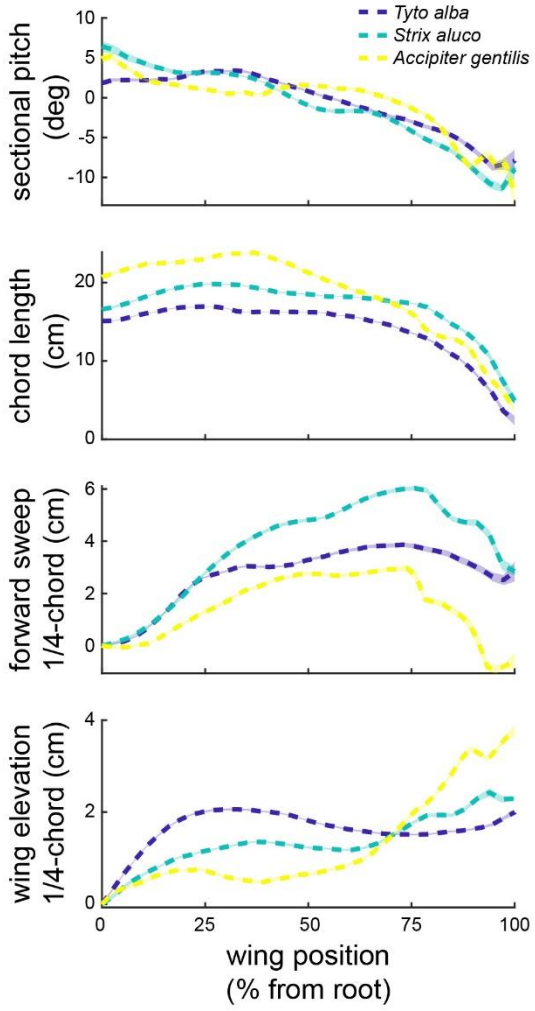


***Figure 27 Distributions along the span of wing pitch, chord length, and the movement of the quarter-chord line.*** *Negative pitch of each wing section indicates the leading edge rising. Dashed lines indicate mean across span. Shaded patched are standard error of the mean. Data are for left and right wings combined.*

*Wing thickness and camber*

Wing thickness was greatest in the region of the wing possessing the articulating bones and actuating muscle (Fig. 28). Within these thick regions of the wing, peak thickness decreased linearly with span over the proximal 2/3 of the wing. Peak average wing thickness was 11.1 ± 0.2%, 10.7 ± 0.2%, and 12.8 ± 0.2% of the chord, and always occurred in the most proximal section, and peaked along the chord at approximately 40% of the chord length in *T. alba*, and 25% in both *S. Aluco* and *A. gentilis*. Distally or near the trailing edge, the wing was thin as expected from the anatomical structure. Our measurements suggested wing thickness of approximately 0.5% of the chord length, i.e., on the order of a millimeter.

Peak wing camber varied across the span and differed across birds (Fig. 29). Peak average camber was 7.0 ± 0.1%, 9.4 ± 0.1%, and 11.1 ± 0.1% of the chord. For all birds, the location of peak camber was near mid-chord, but differed in its spanwise location: approximately 33%, 15%, and 10%. There was also a secondary peak in camber for all birds in the distal half of the wing, which occurred at approximately 60% span, but of lower magnitude than the primary peak. Camber in the distal quarter of the wing was 0.5-3% of the chord length. Mean wing camber was positive throughout the wing.

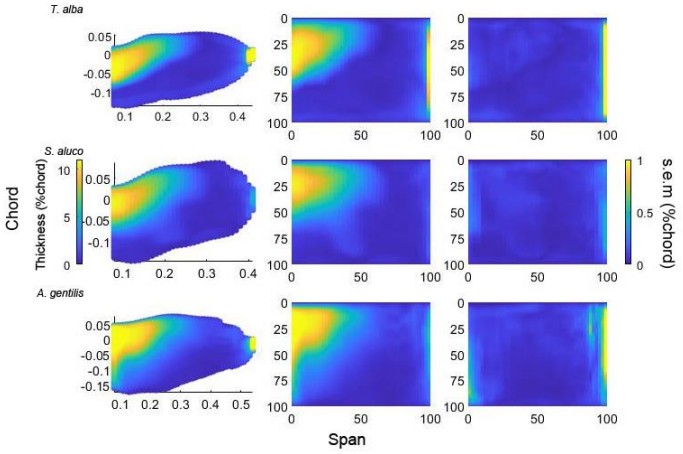


***Figure 28. Average wing thickness and standard error across three birds (rows).*** *Left column) Average planform colour coded by thickness (% chord length). Middle column) Same data as left-column re-mapped to a rectangular planform. Right column) standard error of the mean wing thickness (% chord length).*

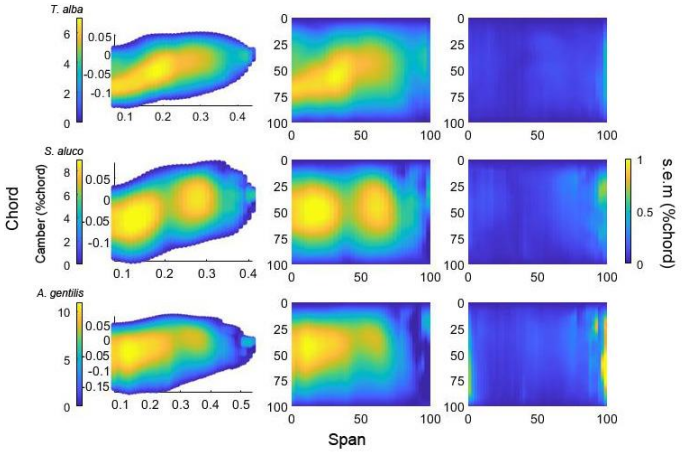


***Figure 29. Average wing camber and standard error across three birds (rows).*** *Left column) Average planform colour coded by camber (% chord length). Middle column) Same data as left-column re-mapped to a rectangular planform. Right column) standard error of the mean wing camber (% chord length).*

*Changes in the mean line with speed*

The patterns of change in mean line displacement with increasing dynamic pressure are similar across all three birds. Changes in the mean line of each chord represent changes in wing twist, ¼-chord movement, and wing camber. Two regions of the wing decrease in height and two regions increase in height. Decreasing in height are 1) the proximal and posterior/aft region of the wing, and 2) the distal wing beyond the wrist in around 30% chord. Increasing in height are 3) the proximal and anterior region of the wing, and 4) the mid-span and posterior/aft region. The coefficients of determination are relatively low (<0.25) across the wing in *T. alba*, but peak in similar locations that align with the four regions of changing mean line height. In *S. Aluco* and *A. gentilis*, each of the four regions peak above 0.60 coefficient of determination. Within those four regions of *S. aluco* and *A. gentilis*, peak change in mean line by region are 1) -0.04 and -0.04; 2) -0.03 and -0.02; 3) 0.05 and 0.04; and 4) 0.07 and 0.05 $cm \cdot Pa^{-1}$, respectively; limiting our analysis to the surface with $r^2$ greater than 0.5. The pattern of shape change is reminiscent of a saddle shape.

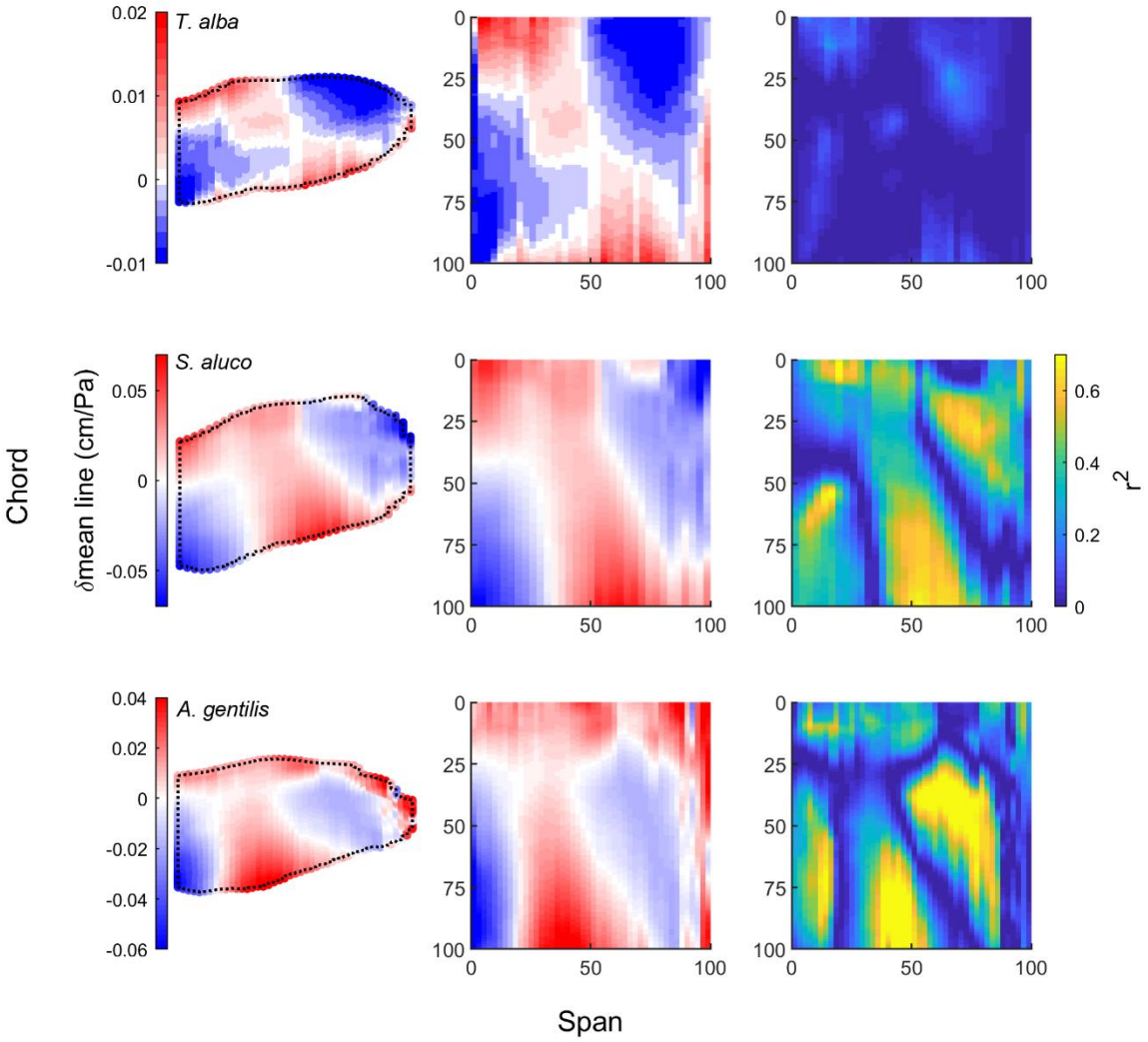


***Figure 30. With increasing dynamic pressure (speed-squared), the mean line of the wing reconfigures in a saddle-like pattern in all three birds (rows).*** *Left column) out-of-plane movement of the mean line mapped to the average wing planform with increasing dynamic pressure. Middle column) Same data as left-column re-mapped to a rectangular planform. Right column) The quality of the linear relation described by the coefficient of determination ($r^2$; theoretical range 0-1).*

## Free-flight data and wing movements

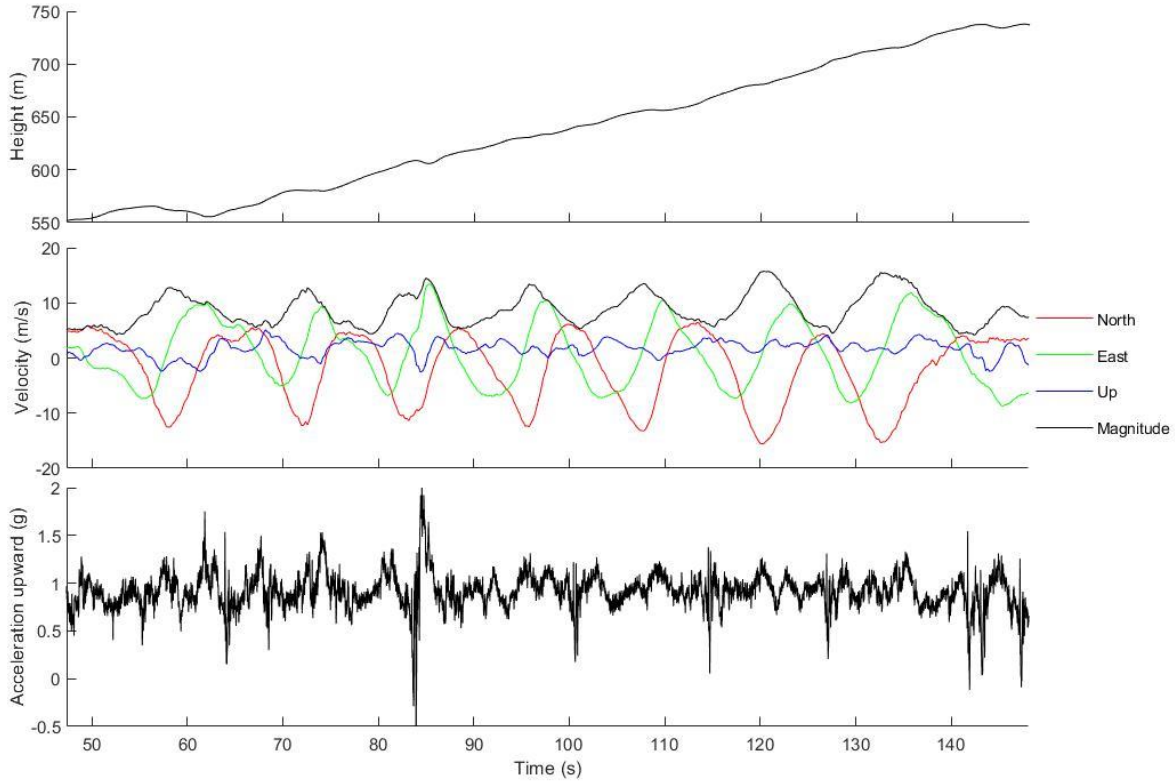


***Figure 31 Free-flight measurements from a Golden Eagle slope soaring.*** *A 100s window of a Golden Eagle slope soaring; circling in to-- and away from-- the wind. Top) ascent in response to the slope soaring behaviour. Middle) ground-speed velocity of the circling behaviour. Bottom) vertical acceleration repeatedly dips in the circling movements.*

The Golden Eagle as it circled consistently experienced a loss in lift, as seen in the acceleration, at approximately the same bearing, and this coincided with a wing tuck in the video. Slope soaring occurs in response to patterns in wind that develop in response to topology. Soaring birds take advantage of these consistent winds to gain elevation (Fig 31, top). When the bird's bearing was NW, it repeatedly experienced a loss in vertical acceleration (acceleration <1 g), and initiated a wing tuck. The next steps are to quantitatively describe the wing kinematics and the effect of the tuck on body accelerations based on the inertial properties of the wings.

| Soaring eagle wing posture | Tucked eagle wing posture |
|---|---|
|  |  |

# 8 Directions for expansion

- Exploring the response of the barn owl to a rotational perturbation. Identifying the recovery movements and the role of inertia and elasticity in rejection of the roll perturbation.

# 9 Publications

- High aerodynamic lift from the tail reduces drag in *Journal of Experimental Biology*
    - Awarded the "most read and talked-about" paper in *J. Exp. Biol.* for 2020. Also it's #1 output ever (of 6,276 recorded articles) according to Altmetric Attention Score as of Mar 2020, and in the 99.99th percentile of all scored research by Altmetric (cob.altmetric.com/details/75737329#score)
- Bird wings act as a suspension system that rejects gusts in *Proceedings of the Royal Society B: Biological Sciences*
- Raptor wing morphing with flight speed in *Journal of the Royal Society Interface*.
- Virtual manipulation of tail postures of a gliding barn owl (*Tyto alba*) demonstrates drag minimisation when gliding in *Journal of the Royal Society Interface*
- Fly low: The ground effect of a barn owl (*Tyto alba*) in gliding flight in *Proceedings of the Institution of Mechanical Engineers C*.
- *in prep*: 1) Dynamics of hinged wings in upgusts; 2) Passive gust rejection in a bio-inspired glider

# 10 Output

- Annual review for "Muscular-Skeletal System Inspired Morphing Air Vehicles Using Active Materials" (A.K.A. Avian-Inspired Wing Morphing) – 2017-20
- Society for Experimental Biology – 2017, 2018, 2019
- Society of Integrative and Comparative Biology – 2018, 2019, 2020
- SOAR meeting - 2017 & 2019
- CoeBit meeting - 2017 & 2018
- NIFTI/SOAR teleconference - 2018, 2019
- iMav - 2018
- ISABMEC - 2018
- Publication†: High aerodynamic lift from the tail reduces drag in *Journal of Experimental Biology*
- † Awarded the "most read and talked-about" paper in *J. Exp. Biol.* for 2020. Also it's #1 output ever (of 6,276) according to Altmetric Attention Score as of Mar 2020, and in the 99.99th percentile of all scored research by Altmetric (cob.altmetric.com/details/75737329#score)

- Publication: Bird wings act as a suspension system that rejects gusts in *Proceedings of the Royal Society B: Biological Sciences*
- Publication: Raptor wing morphing with flight speed in *Journal of the Royal Society Interface*.
- Publication: Virtual manipulation of tail postures of a gliding barn owl (*Tyto alba*) demonstrates drag minimisation when gliding in *Journal of the Royal Society Interface*
- Publication: Fly low: The ground effect of a barn owl (*Tyto alba*) in gliding flight in *Proceedings of the Institution of Mechanical Engineers C*.
- Manuscripts in prep: 1) Dynamics of hinged wings in upgusts; 2) Passive gust rejection in a bio-inspired glider
- Patent for gust rejection mechanism: GB 1903806.6
- Outreach and discussion with Renault formula one racing – 2018; Airbus – 2020; Mercedes AMG formula one racing (postponed from 2020)
- Software development with flow diagnostic company LaVision GMBH
- Invited presentation: Universite Catholique de Louvain (2019)
- Invited presentation: International Conference on Robotics and Automation (Postponed from 2020)